nature communications

Article

https://doi.org/10.1038/s41467-024-54507-4

High performance plain carbon steels obtained through 3D-printing

Received: 19 July 2024

Accepted: 11 November 2024

Published online: 21 November 2024

Check for updates

Qiyang Tan[1,6], Haiwei Chang[1,6], Guofang Liang[1], Vladimir Luzin[2,3], Yu Yin[1], Fanshuo Wang[1], Xing Cheng[4], Ming Yan[4], Qiang Zhu[4], Christopher Hutchinson[5] ✉ & Ming-Xing Zhang[1] ✉

Over the last century, improvement in mechanical performance of structural metals has primarily been achieved by creating more and more complex chemical compositions. Such compositional complexity raises costs, creates supply vulnerability, and complicates recycling. As a relatively new metal processing technique, metal 3D-printing provides a possibility to revisit and simplify alloy compositions, achieving alloy plainification, which enables simpler materials to be used versatilely. Here, we demonstrate that high performance simple plain carbon steels can be produced through 3D-printing. Our 3D-printed plain carbon steels achieve tensile and impact properties comparable, or even superior to those of ultra-high strength alloy steels such as Maraging steels. The sequential micro-scale melting and solidification intrinsic to 3D-printing provides sufficient cooling to directly form martensite and/or bainite, strengthening the steels while maintaining microstructural and property homogeneity without dimensional limitations or heat treatment distortion and cracking. By manipulating 3D-printing parameters, we can tailor the microstructure, thereby control the properties for customized applications. This offers a scalable approach to reduce alloy complexity without compromising mechanical performance and highlights the opportunities for the 3D-printing to help drive alloy plainification.

Engineering alloys, such as steel and aluminium, are structural materials of choice in applications where strength and damage tolerance are required. These alloys have continually been improved over the last century, growing more and more compositionally complex, with thousands of different alloys now available in the market that an engineer or designer can choose from[1–8]. Each composition is tailored for a given set of properties. This huge expansion and increased complexity in the alloy compositions cause large issues for recycling, almost always raises costs due to the alloying elements required, and challenges the security of supply for certain compositions due to the geographical distribution of elemental resources. As a result, there has been growing interest in the plainification of engineering alloys – a concept promoting a much smaller number of simpler compositions that can be used across many applications, with consequential benefits for recycling, re-use, and security of supply[9,10].

The historical explosion in the number and complexity of alloy compositions is easy to understand if we take an example like ferrous materials – steels and cast irons, by far the most common engineering alloys. The demand for higher mechanical performance (e.g., ultra-high strength, wear resistance, etc.) has necessitated increasingly

[1]School of Mechanical and Mining Engineering, The University of Queensland, Brisbane, QLD, Australia. [2]Australian Nuclear Science and Technology Organization (ANSTO), Sydney, NSW, Australia. [3]School of Engineering, The University of Newcastle, Newcastle, NSW, Australia. [4]Department of Materials Science and Engineering and Shenzhen Key Laboratory for Additive Manufacturing of High-performance Materials, Southern University of Science and Technology, Shenzhen, China. [5]Department of Materials Science and Engineering, Monash University, Melbourne, VIC, Australia. [6]These authors contributed equally: Qiyang Tan, Haiwei Chang. ✉e-mail: christopher.hutchinson@monash.edu; mingxing.zhang@uq.edu.au

precise control over microstructure formation. This is usually obtained through greater compositional complexity and depends strongly on the constraints of the available processing technology. For example, high-performance martensitic or bainitic steels, such as those used in gears, are normally highly alloyed to ensure adequate hardenability. This allows them to be cooled relatively slowly from elevated temperatures to avoid quench cracking or geometric distortion while still obtaining the desired martensitic or bainitic microstructures[11,12]. The alloy chemistry is specifically tailored to accommodate processing constraints, such as heat transfer during fabrication, ensuring uniform microstructure and properties throughout the thickness. This tailoring can even result in different alloy compositions depending on the size and shape of the component. In the same spirit, complicated-shaped objects are not directly cast into their final forms due to the challenges of steel casting, even though it would be economically preferential. Instead, they are fabricated with additional machining and sometimes welding. Adding more carbon (and other elements) to produce cast irons allows one to cast more complex-shaped ferrous components, but the mechanical properties are then not suitable for structural applications[12]. The proliferation in alloy chemistries is as much a consequence of processing technology constraints, as it is a desire to access new microstructures to deliver improved properties.

In this context, when new processing technologies begin to be used by industry, it provides an opportunity to revisit and simplify the alloy compositions being used. This is the case now with metal 3D-printing. Whilst not a new group of technologies, their extensive uptake by the industry is relatively recent[13]. Most 3D-printed components are currently fabricated with existing, complex alloy compositions, rather than compositions specifically simplified to be suitable for metal 3D-printing[14–16].

As one of the most popular metal 3D-printing technologies, powder bed fusion (PBF) uses a high-energy laser or electron beam to selectively melt thin layers of metal powder (Fig. 1a). Each layer is meticulously fused in precise locations to form micro-scale melt pools (Fig. 1b), enabling the layer-by-layer construction of complex geometries. Such a micro-scale melting process is renowned for the rapid cooling (10^4 to 10^7 K/s) of the melt pools[13,16]. This is a distinct processing advantage for steels by enabling direct quenching of the component upon manufacturing. Unlike traditional quenching techniques that require rapid cooling of the entire component to obtain the desirable martensite or bainite microstructure, the micro-scale melting and solidification dissects the quenching process into a series of discrete events. Since solidification of a melt pool produces a basic unit of the 3D-printed part, the microstructure of the whole 3D-printed part is mostly defined by the microstructure of the solidified melt pool. This means the localized generation of martensite/bainite within the melt pools ensures much more homogeneous hardening throughout the part, regardless of its size and geometry. That is, PBF circumvents the low hardenability typically associated with plain carbon steels, offering an opportunity to use them as alloy steels with much higher material plainification and simplification.

Here, we demonstrate that by leveraging the intrinsic characteristics of PBF, one of the most popular forms of metal 3D-printing, we can strip out much of the alloy complexity and obtain high mechanical performance and geometric complexity from the simplest imaginable steel chemistry – Fe and C. We demonstrate printing of geometrically complex parts from simple plain carbon steels (Fig. 1c, d) with a wide processing window, uniform through-thickness properties, and tensile and impact properties comparable to, or even superior to low and medium alloy ultra-high strength steels and some Maraging steels. Metal 3D-printing technologies should be at the forefront of alloy plainification strategies.

Results

Hardenability evaluation

Plain carbon steels with carbon contents of 0.4 wt.% (AISI 1040) and 0.8 wt.% (AISI 1080) are chosen as two simple alloys to demonstrate the possibilities. Due to the low hardenability of plain carbon steels, only small parts with simple shapes can be effectively hardened through conventional quenching in water or brine, whereas quenching larger parts or geometrically complicated parts often leads to distortion or cracking, and results in spatially inhomogeneous properties due to significantly reduced internal cooling rates[11,12]. This inhomogeneity is demonstrated by a Jominy End Quench Test on 1080 steel (Fig. 1e), where one end of a cylindrical sample is quenched with a water spray, followed by hardness measurements along its length from the quenched end. As shown in Fig. 1f, only the region within 6 mm from the end achieves a high hardness (~60 HRC) and it decreases quickly away from this region. This behavior is because the martensitic and/or bainitic transformations only take place at the end of the bar due to the low hardenability. The same 1080 plain carbon steel composition has been printed using PBF to create a bar with the same dimensions as the Jominy bar (Method). The measured hardness along the bar is high and uniform across the length (Fig. 1f), indicating the formation of uniform martensite or bainite microstructures. To further demonstrate the performance offered by 3D-printing, even in parts with complex geometries, we printed a 1080 gear-like virtual component (Fig. 1c) with intricate geometry and different thicknesses in the cross-section using PBF (Method). Such geometric complexity poses major challenges for conventional water quenching due to distortions and inability to achieve a uniform hardness. These challenges can be overcome by 3D-printing, as evidenced by the precise geometric accuracy and uniform hardness distribution (~59 HRC) across the entire 3D-printed gear (Fig. 1d). Similar uniform hardness distributions were also achieved in the 3D-printed 1040 steel (Supplementary Fig. 1). It should be emphasised that this gear-like component was not intended for specific practical applications as a gear but rather to demonstrate how 3D-printing can address challenges typically encountered with conventional water quenching of engineering structural parts with complex geometries.

3D-printing of plain carbon steels also enables the avoidance of quench cracking. We prepared two L-shape demonstration parts with the same dimensions. One was machined from commercial 1080 steel, followed by austenization and quenching in water and the other was directly 3D-printed using 1080 steel powder (Method). The water quenching caused distortion and cracking at the corner (Fig. 1g). In contrast, the 3D-printed part was free of cracks and distortion (Fig. 1h). This performance is because the micro-melting dissects quenching into numerous discrete units, effectively compartmentalizing the thermal stress whilst the substrate preheating (Method) and the cyclical thermal profile from the melting of successive layers provides an in-situ tempering effect, reducing the thermal residual stress[13,14]. Notably, while high cooling rates in 3D-printing are essential for martensite and/or bainite formation, the subsequent self-tempering from the cyclic thermal profile does not reach temperatures high enough to revert martensite or bainite to austenite. Instead, it tempers the microstructure, relieving transformation and residual stresses without compromising the benefits of rapid cooling[14]. Thus, the in-situ tempering complements the high cooling rates, enhancing the mechanical performance of the 3D-printed parts.

We also observe that plain carbon steels have excellent 3D-printability, achieving full densification and consistent hardness distribution across parts within a very wide processing window (Fig. 1i, Supplementary Fig. 2 and Supplementary Tables 1 and 2). This not only ensures reliable production quality but also offers the scalability in tailoring their properties using 3D-printing. The hardness of 3D-printed steels varies with the laser energy inputs that determine the cooling rate. A lower energy input correlates with a higher cooling rate of the melt pools, leading to higher hardness[13]. Thus, the 3D-printing processing parameter choice helps provide control over the microstructural characteristics. Manipulating the processing parameters can be used to tailor microstructures and mechanical properties, rendering them highly controllable for customized applications with 3D-printing.

https://doi.org/10.1038/s41467-024-54507-4

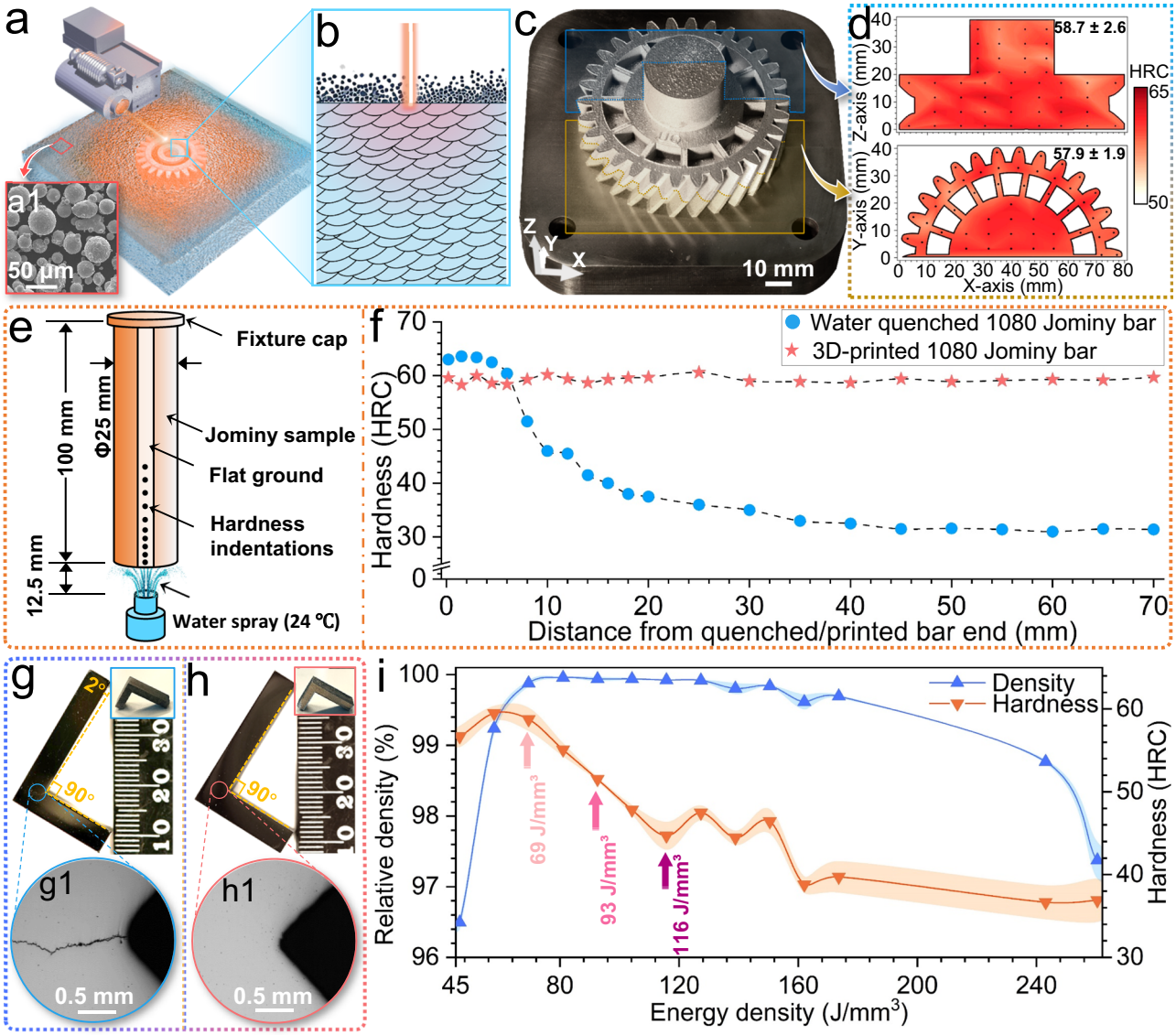

Fig. 1 | Hardenability and metal 3D-printing of plain carbon steel AISI 1080. **a** Schematic illustration of powder bed fusion (PBF) metal 3D-printing process, with the inset (a1) depicting the morphology of 1080 steel powder feedstock, and (**b**) enlarged diagram of the marked area in (**a**), schematically showing the typical fish-scale melt pool structure. (**c**) A bevel gear fabricated by PBF with 1080 steel powder, with the coordinate system showing the plane orientations (Z-axis refers to the building direction). **d** Cross-sectional hardness Rockwell C Scale (HRC) distributions on XZ-plane (upper) and XY-plane (lower) of the bevel gear, indicated by the arrows in (**c**). **e** Schematic illustration of the standard Jominy End Quench Test. **f** Hardness distributions along the conventional wrought 1080 steel bar after Jominy End Quench Test and the 3D-printed 1080 steel Jominy bar. L-shape 1080 steel demonstration parts: (**g**) conventionally water quenched sample, showing quenching distortion and cracking at the sharp corner as demonstrated by (g1) the optical micrograph, contrasted against (**h**) 3D-printed sample with a flawless structure free from distortion and cracking, as demonstrated by (h1) the optical micrograph. **i** Densification behaviors and hardness of the 3D-printed 1080 steel at various laser energy input, showing the excellent printability of this steel. The shaded error bands in (**i**) indicate the standard deviation, calculated as the mean of four tests. The arrows in (**i**) pinpoint the three chosen samples subjected to microstructural characterizations and property validation. Source data are provided as a Source Data file.

Microstructural characterization

To delve deeper into the microstructural and mechanical features, we conducted comprehensive characterizations and validations on selected 1080 and 1040 samples 3D-printed with different processing parameters (energy input density), as indicated in Fig. 1i and Supplementary Fig. 3d. X-ray diffraction (XRD) analysis identifies a single ferritic (α′) phase in our 3D-printed 1080 steels, with no austenite or carbides detected (Fig. 2a). Microstructural examination with electron backscattered diffraction inverse pole figure (EBSD-IPF) mapping demonstrates that the ferrite manifests as fine, plate-like features, uniformly distributed without preferential orientations (Fig. 2b–d). Statistical analysis reveals consistent α′-block sizes, ranging from ~1 μm to ~10 μm with an average size of ~2 μm. The corresponding pole figures (Supplementary Fig. 3) demonstrate an orientation relationship between the α′-blocks and prior γ grains approximating to the Greninger-Troiano relation, which has been reported in martensitic and bainitic steels[17,18]. These results show the occurrence of either martensitic or bainitic transformations during the 3D-printing process, and the suppression of the pearlite transformation for all energy inputs examined.

Grain Average Band Contrast (BC) maps (Fig. 2e–g) were directly derived from the EBSD data to further differentiate martensite and bainite in our 3D-printed 1080 steel (Method). Generally, martensite exhibits relatively lower BC values than bainite[19,20]. In the 1080 sample

https://doi.org/10.1038/s41467-024-54507-4

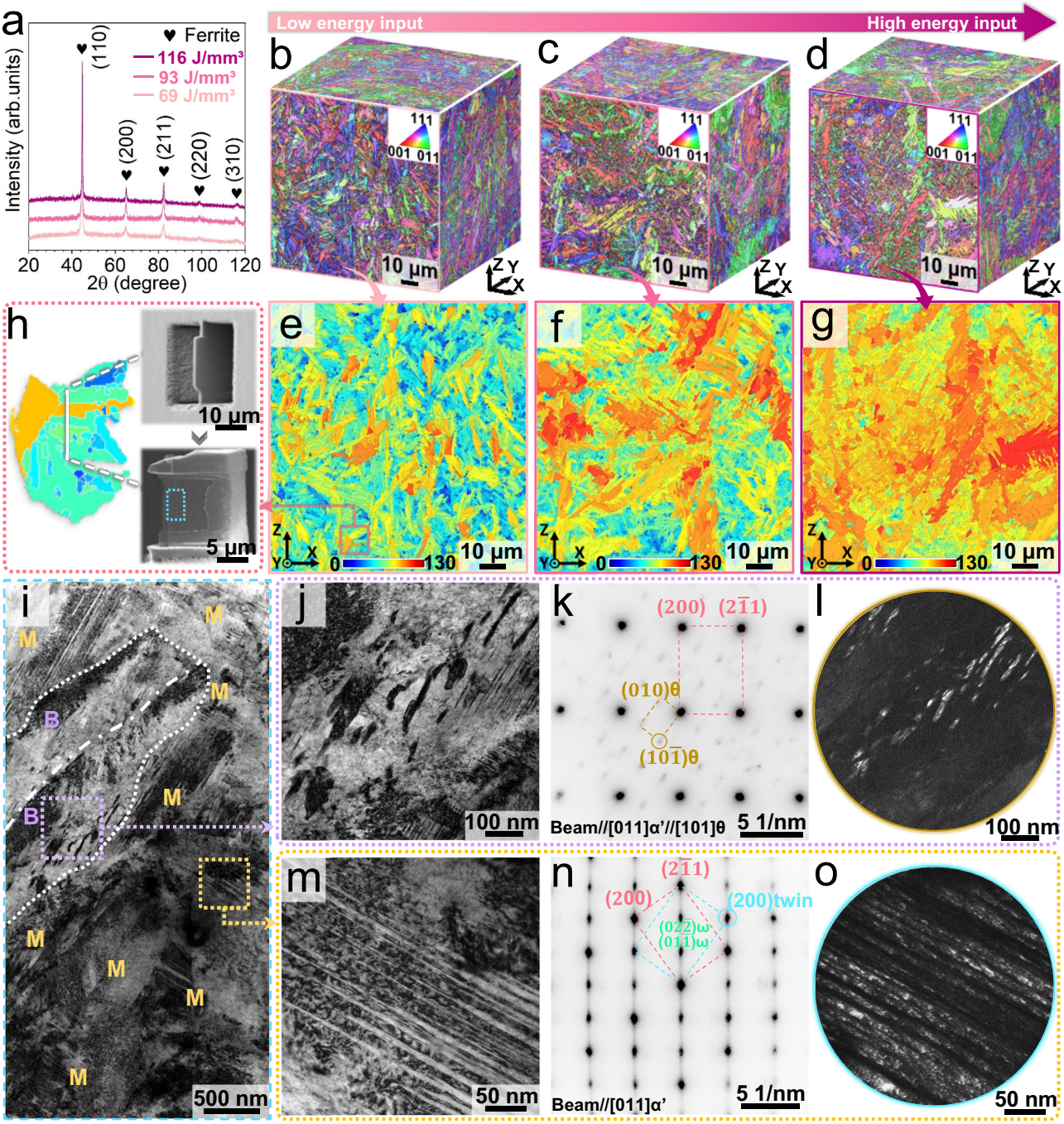

Fig. 2 | Microstructural analysis of 3D-printed 1080 steels. a X-ray diffraction (XRD) spectra. **b**–**d** 3D stereographic electron backscattered diffraction inverse pole figure (EBSD-IPF) maps of samples fabricated with energy inputs of (**b**) 69 J/mm^3, (**c**) 93 J/mm^3, and (**d**) 114 J/mm^3, with coordinate system showing the plane orientations (Z-axis refers to building direction). **e**–**g** Grain Average Band Contrast maps, retrieved from **b**–**d**, respectively. The color scales represent the band contrast (BC) values. **h** Focused-ion-beam lift-out specimen at the marked area in (**e**). **i** Bright-field transmission electron microscopy (TEM) micrograph of the marked areas in (**h**), with the white-dashed line delineating the α′-block with high BC value and labels B and M representing bainitic and martensitic α′-laths, respectively. **j**, **m** Higher magnified TEM images of the areas marked in (**i**), taken close to the $[011]_{\alpha'}$ zone axis. **k**, **n** The diffraction patterns of (**j**) and (**m**), respectively, taken close to the $[011]_{\alpha'}$ axis. **l**, **o** Dark-field TEM images taken from the diffraction spots marked in (**k**) and (**n**), respectively. Source data are provided as a Source Data file.

printed with low energy input (69 J/mm^3), the majority of the α′-blocks exhibit relatively low BC values below 70 (Fig. 2e), indicative of a predominance of martensite with low Kikuchi pattern qualities. Increasing the laser energy input results in a higher fraction of α′-blocks with high BC values over 100. Notably, the sample produced with high energy input (116 J/mm^3) exhibits a microstructure predominantly composed of high BC-valued α′-blocks (Fig. 2g). This implies that an increase in laser energy input prompts a transition from a martensite-dominant to a bainite-dominant microstructure in our 3D-printed 1080 steel.

To further corroborate this differentiation, we employed transmission electron microscopy (TEM) examination of these 1080 samples. As shown in Fig. 2h, a TEM thin foil was lifted out from a region encompassing α′-blocks with both low and high BC values in the low-energy-produced sample using the focused-ion-beam technique. Our TEM observation reveals that individual α′-blocks with high BC value

comprise a series of subdivided α′-laths with submicron widths, showing microstructural characteristic of bainite. The laths exhibit a relative scarcity of lattice imperfections like twins and dislocations but contain nano-sized carbides (Fig. 2i, j). The associated diffraction pattern (Fig. 2k) and high-resolution TEM image (Supplementary Fig. 4a) further confirm the carbide as cementite (θ-Fe_3C) and a well-established orientation relationship between these two phases[21]:

$$[011]_{\alpha'}||[101]_{\theta},\ (\bar{2}1\bar{1})_{\alpha'}||(30\bar{3})_{\theta}$$

This is a different format of the Isaichev orientation relationship[22]. These results evidence a typical bainite feature of this α′-block, consistent with its high BC value.

In contrast, α′-laths in the low BC blocks are devoid of cementite and exhibit a nano-twinned substructure (Fig. 2i). These twins possess widths ranging from 10 to 30 nm (Fig. 2m) and a typical {112}<111> – type twining mode, verified by the corresponding diffraction pattern (Fig. 2n). In addition to the diffraction spots from the α′-matrix and α′-twin, we also observed extra weak $(1\bar{1}0)_{\omega}$ and $(2\bar{2}0)_{\omega}$ spots that belong to ω-Fe phase. High-resolution TEM (Supplementary Fig. 4b) demonstrates that the ω-Fe phase has a thickness of several atomic layers, distributing along the twin boundaries. The ω-Fe is known as a metastable interfacial-twin-boundary phase that commonly forms in twinned martensite to alleviate stress concentrations and minimize interfacial energy[23–25]. These observations demonstrate high-carbon martensite in the sample, consistent with its low overall BC value (Fig. 2e).

In addition to the martensite-dominant microstructure in samples produced with low energy input, TEM analysis of the high-energy-produced 1080 steel sample reveals a bainite-dominant microstructure (Supplementary Fig. 5), consistent with its elevated overall BC value shown in Fig. 2g. Compared with martensite, bainite is characterized with a mix of bainite α′-phase with lower carbon supersaturation and θ-Fe_3C nanoparticles[12]. In contrast to classic bainite with coarse carbides in conventionally processed high carbon plain steels, the bainite in our 3D-printed 1080 steel features nanometer-sized cementite. This can be ascribed to the fast cooling intrinsic to the micro-scale melting and solidification process.

Similar to the 1080 steel, a single ferrite phase is observed in the 3D-printed 1040 steels (Fig. 3a) and the pearlitic transformation was fully suppressed (Fig. 3a–d). However, achieving a martensite-dominant microstructure in 1040 steel is more challenging than in the 1080 steel even with low energy input. This is evidenced by the Grain Average Band Contrast maps (Fig. 3e–g) and the complementary TEM characterization (Fig. 3h–n). As shown in Fig. 3e, the sample produced with a lower energy input of 69 J/mm^3 still contains α′-blocks with high BC values that is greater than 100, interspersed with some low BC-valued α′-blocks. This indicates a microstructure mixed with both bainite and martensite, with the former being dominant. This is due to the lower carbon content of the 1040 steel, which is associated with lower martensitic hardenability, favouring the bainite formation[12]. Nevertheless, such bainitic microstructures distinguish themselves by hosting nano-scale α′-laths (Fig. 3i) interspersed with a few nano-sized, metastable ω′-carbides (Fig. 3j, k) rather than the high fraction of coarser needle or particulate cementite typical of conventional bainite commonly observed in plain carbon steels[12]. This is due to the suppression of cementite growth by rapid cooling and substantial remaining carbon supersaturation within the bainitic α′-laths during the 3D-printing process. Such a condition favors bainite formation at lower temperatures, resulting in finer bainite laths. While the microstructure predominantly consists of bainite, regions of {112}<111> – type twinned martensite are also present in the sample (Fig. 3l–n).

Increasing the laser energy input results in a higher fraction of α′-blocks with high BC values over 100 (Fig. 3f, g). At the energy input of 127 J/mm^3 (Fig. 3g), a full bainite microstructure is obtained. Our TEM (Supplementary Fig. 6) further confirms that, unlike the nanostructured bainite formed in the low-energy-produced samples, bainite formed in the high-energy-produced sample contains coarser carbides even though the α′-laths are still at nanometer scale.

Mechanical performance

We performed tensile testing and Charpy impact testing (Fig. 4) to evaluate the basic mechanical performance of the 3D-printed 1080 and 1040 plain carbon steels. The determined yield strength (YS), ultimate tensile strength (UTS), elongation to fracture (El) and impact toughness are summarized in Supplementary Table 3. Like all conventionally fabricated martensitic steels, tempering is necessary for 3D-printed 1080 steels due to the formation of martensite. Our as-printed 1080 samples were tempered at 300 °C for 2 h before mechanical testing to reduce residual stresses and to mitigate the intrinsic brittleness of fresh martensite. Note that this tempering temperature may not be optimal for these steels, whereas a more suitable tempering process for a particular 3D-printed carbon steel can be optimized in the future in terms of actual application requirements. For the 1040 steel, we found that good strength-ductility-toughness trade-off can be achieved directly after 3D-printing, alleviating the need of heat treatment. This is due to the auto-tempering effect typical of bainitic transformation (Supplementary Section 8). Thus, the mechanical performance of 1040 steel discussed here is focused on the as-printed condition.

Benefiting from the high-carbon martensite, the plain carbon 1080 steel fabricated with low energy input exhibits a yield strength of 1773 MPa and a tensile strength of nearly 2000 MPa (Fig. 4a). However, the associated elongation and impact toughness were 5.3% and 8 J, respectively. Increasing the laser energy input prompts a transition from martensitic to bainitic microstructure (Fig. 2e–g). Compared with martensite, bainite is characterized with a mix of bainite α′-phase with lower carbon supersaturation and θ-Fe_3C nanoparticles (Supplementary Fig. 5), providing a configuration that is a little softer but more resistant to crack propagation[12]. Specifically, the YS, UTS, El and impact toughness of the 1080 steel fabricated with high energy input were determined to be 1100 MPa, 1327 MPa, 13% and 22 J, respectively.

The formation of martensite in our 3D-printed plain carbon steels opens the opportunity to further enhance the properties through post heat-treatment. We further conducted microstructural characterization and mechanical tests (Supplementary Figs. 7–9 and Supplementary Table 3) on the 3D-printed 1080 steel after tempering at various temperatures. Increasing the tempering temperature facilitates the transition of fresh high-carbon martensite to a typical tempered high-carbon martensite characterized by detwinning and the formation of a high fraction of nano-sized carbides. This provides access to other strength-ductility-toughness combinations. For example, tempering at 350 °C for 2 h led to a mechanical profile in the low-energy-produced 1080 steel, with an YS of 1533 MPa, UTS of 1726 MPa, El of ~10% and toughness of 11 J.

Properties of the 3D-printed 1040 steels are also sound (Fig. 4b). The sample produced with low energy input achieved an YS of 1340 MPa, UTS of 1430 MPa, El of ~10% and impact toughness of 30 J. Increasing the laser energy input led to a reduction in YS to 1000 MPa and UTS to 1100 MPa, while enhancing El and impact toughness to approximately 14% and 106 J, respectively. Notably, these properties were achieved directly after 3D-printing, and subsequent tempering treatments had only a marginal effect on the mechanical performance of this steel (Supplementary Fig. 9). 3D-printed materials typically require post heat-treatments to release the residual stress and homogenize the microstructure, thereby optimize strength-ductility trade-off[13]. The impressive as-printed mechanical performance of the 1040 steel highlights the convenience and efficacy of 3D-printing for fabricating this steel, alleviating the need for subsequent heat treatment.

https://doi.org/10.1038/s41467-024-54507-4

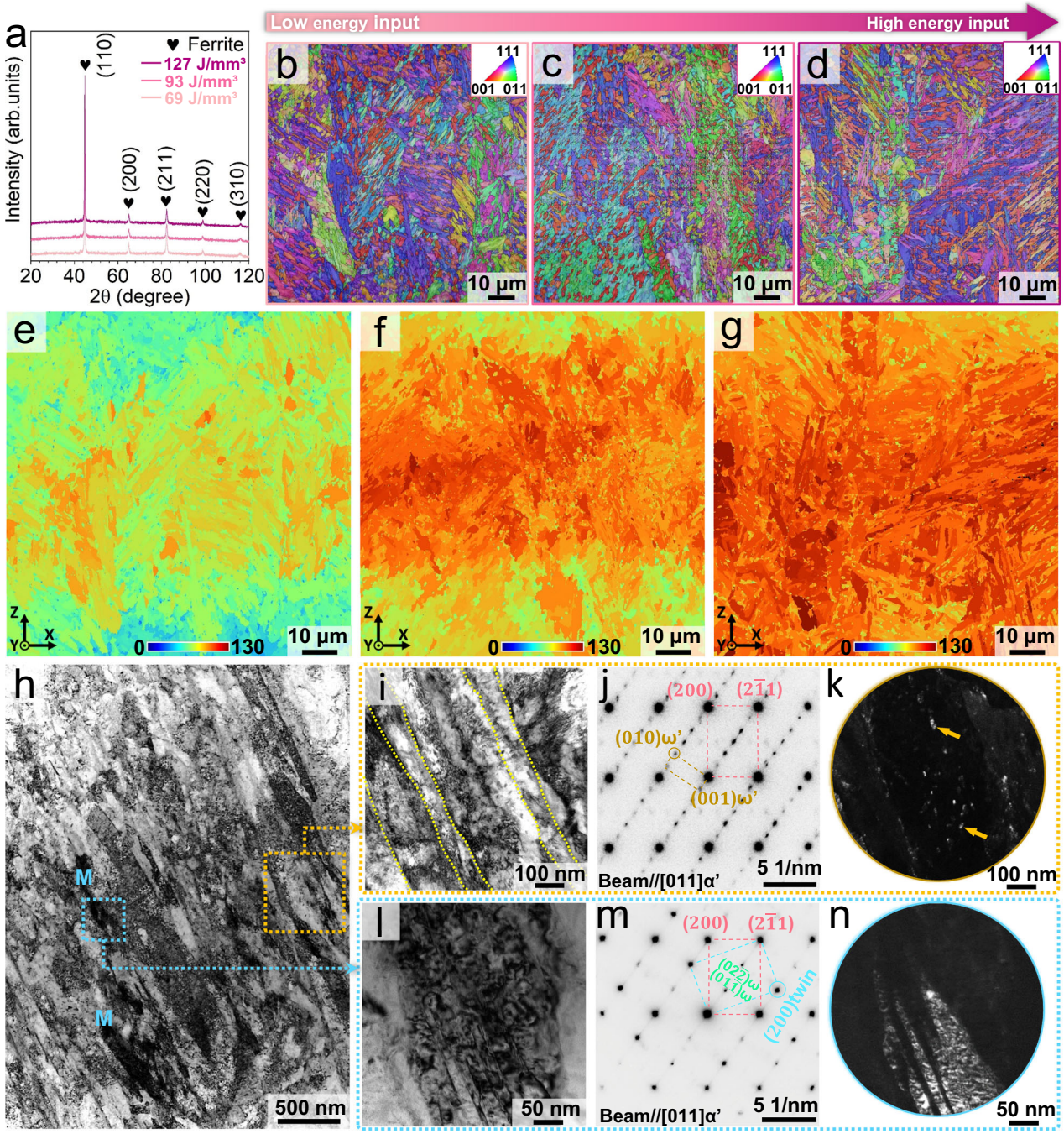

Fig. 3 | Microstructural analysis of 3D-printed 1040 steels. a X-ray diffraction (XRD) spectra. **b**–**d** Longitudinal electron backscattered diffraction inverse pole figure (EBSD-IPF) maps of samples fabricated with energy inputs of (**b**) 69 J/mm^3, (**c**) 93 J/mm^3, and (**d**) 127 J/mm^3. **e**–**g** The corresponding Grain Average Band Contrast maps, retrieved from (**b**–**d**), respectively. The color scales represent the band contrast (BC) values. **h** Bright-field transmission electron microscopy (TEM) micrograph of the low-energy-produced sample, with the label M representing martensitic α′-laths. Magnified views of the marked areas in (**h**), showing typical (**i**) bainite α′-laths and (**l**) martensite α′-laths. The yellowish dashed lines in (**i**) indicates lath boundaries. **j**, **m** The diffractions patterns of (**i**) and (**l**), respectively, taken along the $[011]_{\alpha'}$ axes. **k**, **n** Dark-field TEM images taken from the diffraction spot marked in (**j**) and (**m**), respectively. The arrows marked in (**k**) shows ω′-Fe_3C nanoparticles. Source data are provided as a Source Data file.

To compare the mechanical properties of the 3D-printed plain carbon steels with conventional wrought steels of the same grade, Fig. 4c, d present Ashby plots showing the combinations of yield strength and elongation, and yield strength and impact energy[26–33]. Owing to the inherent low hardenability, large wrought parts made of 1080 and 1040 steels primarily exhibit pearlite or ferrite-pearlite microstructures, characterized by their limited strength[12]. In particular, the conventional wrought 1080 steel even shows an impact toughness less than 10 J due to the coarse pearlitic carbides that facilitate crack propagation[27,28,34]. In comparison, the emergence of ultrafine martensite and bainite structures in our 3D-printed samples delivers an improved strength-ductility-toughness synergy outperforming their wrought counterparts.

A comparison with conventional wrought alloy steels (Fig. 4e, f) demonstrates that the 3D-printed plain carbon steels exhibit strength-ductility-toughness combinations comparable with many highly

https://doi.org/10.1038/s41467-024-54507-4

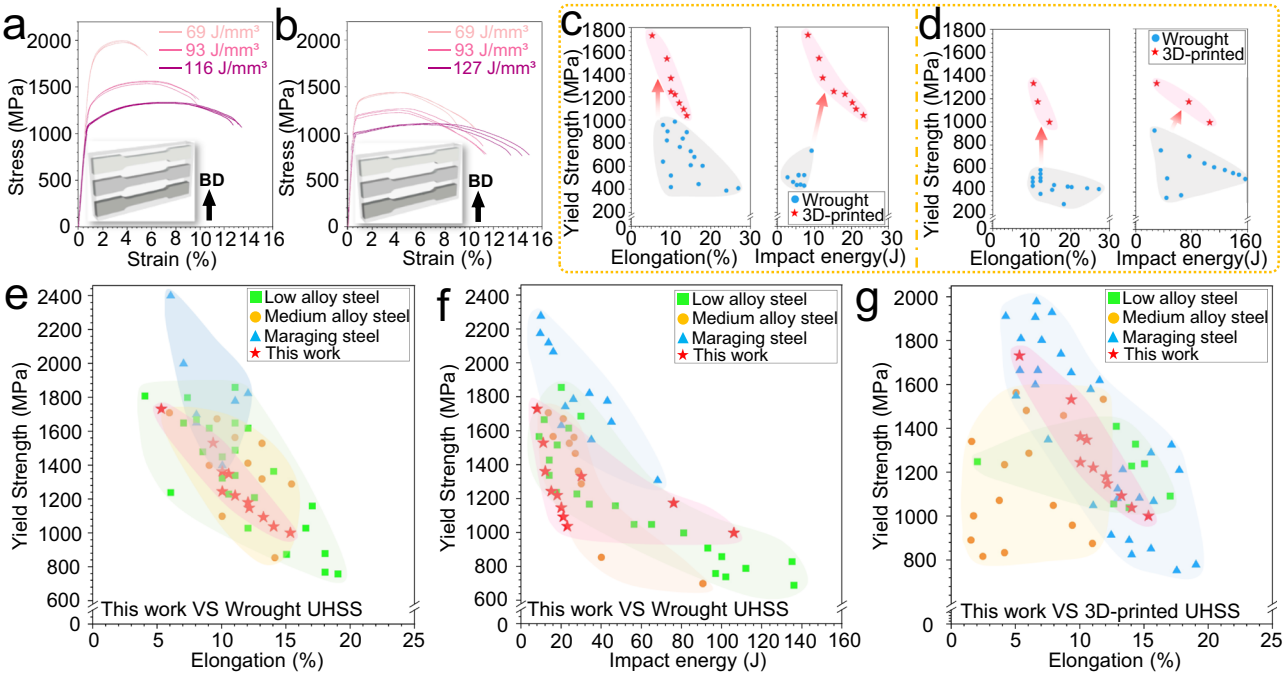

Fig. 4 | Mechanical properties. Typical engineering tensile stress-strain curves of the 3D-printed (**a**) 1080 steels and (**b**) 1040 steels at different laser energy inputs, with insets and arrows showing the sample sectioning orientation and building direction (BD), respectively. Ashby plots illustrating mechanical properties of 3D-printed (**c**) 1080 and (**d**) 1040 steels in comparison with their conventionally wrought counterparts[26–33]. Ashby plots comparing mechanical properties of 3D-printed plain carbon steels against typical commercial ultra-high strength steels (UHSS) manufactured by (**e**, **f**) wrought and (**g**) 3D-printing, as reported previously[14,27,35–41]. The commercialized steels in (**e**–**g**) includes 4130, 4140, 4340, 8640, and 300 M as typical low alloy UHSS, H11 and H13 as typical medium alloy UHSS, and 18Ni(200), 18Ni(250) and 18Ni(300) maraging steels. The shaded bands in these Ashby plots show the populated areas, derived from the corresponding data distributions. Note that the data of the 3D-printed plain carbon steels in these Ashby plots were selected from Supplementary Table 3 to effectively illustrate the distribution of the achievable properties while avoiding excessive data overlap. The full data for all properties at different processing conditions is listed in Supplementary Table 3. Source data are provided as a Source Data file.

alloyed ultra-high strength steels (UHSS) after standard heat treatments, such as 4340, 8640 and 300 M low alloy steels, and H11 and H13 medium alloy steels[27], and are even close to maraging steels[27,35]. This comparison particularly demonstrates that in PBF, compositional complexity is not required for high mechanical performance and the simple composition of the 1040 and 1080 steels offers significant sustainability and cost-saving advantages compared to the heavily alloyed steels.

The current activities on 3D-printing of structural steel in the research community are mostly focussed on highly alloyed UHSS such as H13, 4340, and Maraging steels[14,36]. The strength of these alloy steels primarily arises from the formation of ultrafine martensite or bainite microstructure, but this can be obtained in 3D-printed plain carbon steels. Notably, in some alloy steels, the high level of alloying element additions can lead to pronounced solute segregation and the formation of cellular structures under rapid solidification conditions during 3D-prinitng[13]. These structures can strengthen the steel by providing effective grain boundaries that impede dislocation movement. However, significant solute segregation may also result in the formation of brittle phases at the cell boundaries, decreasing ductility and toughness. A typical example is the formation of mechanically unstable retained austenite networks in the 3D-printed H13 steels[37]. In contrast, the plainified composition of carbon steels circumvents this issue while capitalizing on rapid cooling to facilitate steel hardening. As a result, 3D-printed plain carbon steels attain a favorable combination of strength and ductility, which are comparable or even superior to some 3D-printed UHSS, as shown in Fig. 4g[14,36,38–41].

To further understand the superior mechanical performance of the 3D-printed plain carbon steels, the underlying strengthening mechanisms are briefly discussed. The strengthening of steels generally includes contributions from lattice friction, solid solution, precipitation, dislocations, and effective grain boundaries[12]. In the 3D-printed 1080 and 1040 steels, the formation of martensite and bainite with hierarchical nano-sized substructures provides substantial boundaries, which act as effective barriers to dislocation motion. Due to the shear formation mechanism, martensite and bainite, particularly the former, are typically carbon supersaturated. This leads to severe lattice distortions, raising energy barriers against dislocation propagation within the α′-blocks. Furthermore, TEM observations reveal numerous nano-sized carbides within the bainite and tempered martensite microstructures, as shown in Figs. 2 and 3, and in Supplementary Figs. 5–8. These carbides further enhance precipitation hardening by suppressing dislocation movement.

Discussion

Our work demonstrates the potential of transforming plain carbon steels into high-performance materials through metal 3D-printing. The fast cooling during micro-scale melting can effectively inhibit pearlite formation in plain carbon 1040 and 1080 steels within a broad 3D-printing processing window. By strategically manipulating the 3D-printing parameters, we can achieve microstructure customization in these steels, enabling a choice between ultrafine martensitic or bainitic microstructures that offer properties comparable to UHSS. This is equivalent to the outcomes achieved by complex and extensive alloying strategies but with significantly increased material plainification and simplification. Although achieving a martensite-dominant microstructure in 1040 steel is more challenging than in 1080 steel, the fast-cooling rate at the low energy input allows the formation of nanostructured bainite in the 1040 steel. Such a microstructure resembles those of nano-bainitic steel[42–45] rather than the conventional

bainite[12]. Typically, nano-bainitic steels require a precise alloying strategy through incorporating significant amounts of substitutional solutes such as Si, Mn, Mo, Cr and Ni to inhibit cementite formation and enable bainite transformation at lower temperatures[43]. Our findings demonstrate an alternative way to obtain nano-bainite in plain carbon steels via 3D-printing. This underscores an additional benefit of micro-scale melting in metal 3D-printing beyond the direct quenching effect, potentially simplifying the manufacturing of high-performance steel components. This may also widen the applications of metal 3D-printing technologies.

While 3D-printing offers high flexibility to craft tailored microstructure, it generally subjects materials to directional solidification conditions due to the large thermal gradients within the melt pools[13]. This often results in the epitaxial columnar grain growth and a pronounced texture as commonly observed in austenitic steels, titanium and aluminium alloys[46–50]. In the case of plain carbon steels, the martensitic and bainitic transformations mitigate this effect. These transformations create multiple α'-blocks with different crystallographic orientations within a single prior austenite grain, effectively counteracting the typical columnar structures and texture formed during directional solidification[14]. The resulting ultrafine, almost texture-free microstructures of our 3D-printed plain carbon steels (Figs. 2 and 3) are testament to this mechanism. This microstructural refinement also contributes to the reduction in property anisotropy, addressing a common issue in 3D-printed alloys with columnar grains, as demonstrated by Supplementary Fig. 10 which compares the tensile responses of horizontally and vertically printed samples.

This work demonstrates that very high mechanical performance can be obtained in 3D-printed plain carbon steels. Large alloying additions are not required for high mechanical performance from 3D-printed metallic components, with consequential benefits on cost, recyclability, and security of supply of materials required for these components. The promising properties achieved in the 3D-printed plain carbon steels underscore the imperative need for future work in this domain, particularly in other properties such as fatigue resistance, fracture toughness, and stress corrosion cracking. Naturally, improving properties like corrosion resistance will require the addition of elements such as chromium, while other strategic alloying elements may be necessary for specific properties such as oxidation resistance. The principle remains to add complexity to the composition only when absolutely necessary. Such developments align closely with the ongoing focus on material sustainability and plainification, positioning metal 3D-printing as versatile and forward-looking choices in the evolving landscape of materials technology.

Methods

Powder feedstock preparation

Gas-atomized spherical pure iron powder with commercial purity (99.5 wt.%) and size of 15−-53 µm, and AISI 1080 steel powder with size ranging from 10-60 µm were sourced from Changsha Tijo Metal Material Co., Ltd. These powders served as the raw material for our 3D-printing processes. The 1080 powder has chemical composition of 0.8 wt.% C, 0.4 wt.% Si, 0.8 wt.% Mn and Fe (balance), determined by inductively coupled plasma atomic emission spectroscopy. The 1040 steel powder feedstock was prepared by mixing pure iron powder and 1080 steel powder using mechanical agitation process in a TURBULA® shaker mixer for 2 h.

SEM micrographs (Supplementary Fig. 11) reveal that both feedstock powders have numerous satellites on their surfaces. This satelliting effect is commonly observed in gas-atomized metal powders, resulting from collisions between small particles and incompletely solidified larger droplets[51]. Despite this, the powder showed excellent flowability during the printing process.

Materials processing

Both 1080 and 1040 steels were produced in a SLM125HL laser powder-bed-fusion 3D-priting system (SLM Solutions Group AG). The machine is equipped with an ytterbium fiber laser with a wavelength of 1.06 µm and a maximum power of 400 W. Samples were built onto a 316 L steel platform preheated to 200 °C and the building process was performed under an inert and high purity (≥99.99%) argon atmosphere, maintaining an oxygen concentration below 0.05 vol.%. A series of 10 mm × 10 mm × 10 mm cubic samples were fabricated at different processing parameters, listed in Supplementary Table 1, for evaluating the 3D-printability of each steel. These variables were integrated into the volumetric energy density (E, J/mm^3), with $E = \frac{P}{vht}$ for easier comparison, as listed in Supplementary Table 2. After optimization of the processing window, selected processing parameter sets were also used to fabricated large-sized samples for testing tensile properties, Charpy impact toughness, and hardness distribution as detailed in the following sections.

Densification and hardness measurements

The 3D-printability of these plain carbon steels was assessed by the sample densification through image analysis method using the ImageJ software (Version 1.52a) as per the procedure outlined in our previous work[52]. Samples were sectioned along the longitudinal direction, i.e., building direction (BD), from the 3D-printed cubic blocks, followed by mechanical grinding and polishing down to 0.04 µm colloidal silica suspension to obtain the appropriate surface finish. The densification behavior of each sample was examined using a Reichert-Jung POLYVAR MET optical microscope. For each sample, four cross-sectional images were captured to perform statistical analysis to ensure the reproducibility.

Rockwell hardness measurements, employing a load of 1.5 kN, were also conducted on the cubic samples to assess the hardness achieved under different processing parameters. These hardness values served as indicators for selecting appropriate processing parameters for subsequent microstructural analysis and property validation. For each sample, four hardness tests were conducted to ensure the reproducibility.

Hardenability testing

We performed the Jominy End Quench Test to evidence the low hardenability of plain carbon steels. A cylindrical specimen with a diameter of 25 mm and length of 100 mm was sectioned from a wrought 1080 steel bar, supplied by Baosteel Group. The specimen was austenitized at 900 °C for 30 min and then subjected to the standard Jominy End Quench Test as per the procedure outlined in the ASTM A255 standard (Fig. 1e). After the specimen cooled to room temperature, shallow flat ~0.4 mm deep was ground along its length for hardness testing. Rockwell hardness measurements with a load of 1.5 kN were taken along the ground flat, starting from the quenched end up to a distance of 70 mm. Hardness readings were recorded at intervals of 1.5–2 mm within the initial 20 mm, and thereafter 5 mm intervals for the remaining length.

To demonstrate the superior performance of 3D-printing in achieving steel hardening and microstructure homogeneity, a Jominy bar was 3D-printed using the 1080 steel powder with the laser power of 150 W and scanning speed of 600 mm/s (i.e., energy density of 69 J/mm^3). Then the hardness profile was measured using the same method as stated above. In addition, to show the advantage of 3D-printing in producing parts with shape complexity while also achieving both microstructural and property homogeneity for plain carbon steels, a bevel gear with an overall height of 40 mm and a diameter of 80 mm was manufactured using the 1080 steel powder with the optimized parameter set consisting of laser power of 150 W and scanning speed of 600 mm/s. This gear was deliberately designed with intricate

geometry and varied thickness from 1 mm to 80 mm to demonstrate the challenges in achieving uniform hardness that are typically encountered with conventional quenching. The 3D-printed gear was sectioned from both longitudinal and transverse directions, followed by Rockwell hardness measurements taken on each cross-section at intervals of 3–4 mm.

Quenching distortion and cracking testing

To demonstrate that 3D-printing also enables avoiding of quenching cracking and distortion of plain carbon steels, we prepared two L-shape demonstration parts with the same dimensions: lengths of 30 mm (horizontal) and 20 mm (vertical), width of 10 mm and thickness of 5 mm. One was machined from commercial 1080 wrought steel, followed by austenization at 900 °C for 30 min and quenching in water, and the other was directly 3D-printed using 1080 steel powder with the laser power of 150 W and scanning speed of 600 mm/s (i.e., the low-energy-input of 69 J/mm^3 for martensitic microstructure). The sample was built horizontally with its wall (i.e., the thickness side) attached to the substrate. The cross-section of each sample was characterized using a digital camera and optical microscopy to determine the geometric integrity.

Microstructural characterization

The phase analysis of the 3D-printed steels was performed using XRD in a Bruker D8 Advanced Powder X-ray diffractometer, operated at 40 kV and 40 mA. The scan rate of 1° /min and a step size of 0.02° were used at diffraction angle 2θ ranging from 20° to 120°. All XRD scans were performed on the longitudinal planes of the 3D-printed steels.

A JOEL 7800 field emission scanning electron microscope (FESEM), equipped with electron backscattered diffraction (EBSD), was used to characterize the morphology of the feedstock powders and the microstructures of the 3D-printed steels. Metallographic samples were cut from the 3D-printed samples along the longitudinal direction, followed by mechanically grinding and polishing with 0.04 µm colloidal silica suspension to obtain the appropriate surface finish. The α′-block morphology and texture of each steel were characterized using EBSD with a step size of 0.13 µm. Block boundaries were identified with a critical misorientation angle of 15°. Statistically determined average α′-block size was expressed with the circle equivalent diameters (d_{equal}) of the block areas measured from the EBSD-inverse pole figure (IPF) maps using the AZtecCrystal software. The d_{equal} of each α′-block is defined as the diameter of a circle with an equal block area (A), calculated by $d_{equal} = 2\sqrt{\frac{A}{\pi}}$.

Grain Average Band Contrast (BC) maps were derived directly from EBSD data to evaluate the Kikuchi patterns quality and thereby to qualitatively differentiate martensite and bainite in the steels. Generally, martensite contains a higher density of lattice imperfections (e.g., solute saturation, dislocations, twins, and low-angle boundaries) than bainite[12], influencing the Kikuchi diffraction. Therefore, at identical EBSD scanning conditions, the Kikuchi patterns from martensite appear comparatively dimmer and blurrier than those from bainite, leading to relatively lower BC values for martensite[19,20]. While this method is not universally applicable for an accurate differentiation between martensite and bainite due to the dimensionless nature of BC value and the sensitivity of the phase-identification threshold to EBSD analysis and sample conditions, it nonetheless offers valuable qualitative insights when comparing parallel experimental results.

A Hitachi HF5000 transmission electron microscope (TEM), equipped with a probe aberration corrector and operated at an acceleration voltage of 200 kV, was used to further characterize the microstructure of the 3D-printed steels. Selected area electron diffraction (SAED) technique was applied to determine the orientation relationship (OR) between adjacent phases. High-resolution TEM (HRTEM) and fast Fourier transforming (FFT) techniques were used to examine the atomic matching and OR between adjacent phases. The HRTEM images presented herein were post-processed by inverse fast Fourier transforming (IFFT) using the Gatan DigitalMicrograph™ to reduce noise. TEM foils were prepared in a FEI Dual FIB/SEM-SCIOS focused ion beam (FIB) milling system.

Mechanical testing

Specimens for tensile and Charpy impact toughness testing were initially fabricated as blocks measuring 40 mm (width) × 12 mm (thickness) × 25 mm (height) and 55 mm (width) × 12 mm (thickness) × 40 mm (height), respectively. Prior to sample sectioning, some blocks were undergone direct tempering at 300 °C, 350 °C, and 400 °C to alleviate residual stresses and reveal the effect of different tempering temperatures on their microstructures and mechanical performances.

For tensile testing, dog-bone samples with gauge dimensions of 12.5 mm (length) × 3 mm (width) × 2 mm (thickness) were sectioned horizontally from the tensile blocks using electro-discharge machining. Tensile tests were carried out at a constant crosshead velocity of 1 mm/min in an Instron 5584 machine, equipped with a video extensometer to measure the strain until fracture. For each steel at each tempering condition, three samples were tested to ensure reproducibility.

To evaluate the property anisotropy, additional tensile tests were conducted along the vertical direction (i.e., the build direction) on the as-printed 1040 steel. Tensile dog-bone samples with the same dimensions were sectioned vertically from the initially fabricated blocks measuring 25 mm (width) × 12 mm (thickness) × 40 mm (height).

Charpy v-notch impact toughness specimens were machined from the corresponding blocks into 55 mm (length) × 10 mm (width) × 10 mm (thickness) standard Charpy impact test specimens with ASTM E23-07a type A notch. Testing of these specimens was conducted at room temperature using a Mohr Federhaff A.G. (PSW 30) pendulum impact testing machine. Similar to the tensile tests, three samples for each steel and tempering condition were assessed to ensure reproducibility.

Statistics & reproducibility

No statistical method was used to predetermine sample size. All data were included in the analyses, and no data points were excluded. Sample sizes for mechanical and microstructural tests were chosen based on standard practice in materials science to ensure reliable measurements. Each test (e.g., densification, hardness, tensile, and Charpy impact) was repeated 3–4 times to confirm reproducibility.

Data availability

The experimental data generated in this study have been deposited in Figshare[53]. Source data are provided with this paper.

References

1. Hadfield, R. A. *Manganese-steel: I. Manganese in its application to metallurgy: II. Some newly-discovered properties of iron and manganese*. (Institution, 1888).
2. Rashid, M. High-strength, low-alloy steels. *Science* **208**, 862–869 (1980).
3. Raabe, D. et al. Nanoprecipitate-hardened 1.5GPa steels with unexpected high ductility. *Scr. Mater.* **60**, 1141–1144 (2009).
4. Lo, K. H. et al. Recent developments in stainless steels. *Mater. Sci. Eng. R.* **65**, 39–104 (2009).
5. Jiang, S. et al. Ultrastrong steel via minimal lattice misfit and high-density nanoprecipitation. *Nature* **544**, 460–464 (2017).
6. He, B. B. et al. High dislocation density–induced large ductility in deformed and partitioned steels. *Science* **357**, 1029–1032 (2017).
7. Li, Y. et al. Ductile 2-GPa steels with hierarchical substructure. *Science* **379**, 168–173 (2023).
8. Sun, B. et al. Chemical heterogeneity enhances hydrogen resistance in high-strength steels. *Nat. Mater.* **20**, 1629–1634 (2021).

9. Raabe, D. et al. Strategies for improving the sustainability of structural metals. *Nature* **575**, 64–74 (2019).
10. Li, X. et al. Improving sustainability with simpler alloys. *Science* **364**, 733–734 (2019).
11. Bhadeshia, H. et al. *Steels: microstructure and properties* (Butterworth-Heinemann, 2017).
12. Callister Jr, W. D. et al. *Materials science and engineering an introduction* (John Wiley & Sons, 2007).
13. DebRoy, T. et al. Additive manufacturing of metallic components – Process, structure and properties. *Prog. Mater. Sci.* **92**, 112–224 (2018).
14. Yin, Y. et al. Laser additive manufacturing of steels. *Int. Mater. Rev.* **67**, 487–573 (2022).
15. Zhu, Z. et al. Recent progress on the additive manufacturing of aluminum alloys and aluminum matrix composites: Microstructure, properties, and applications. *Int. J. Mach. Tools Manuf.* **190**, 104047 (2023).
16. Su, J. et al. Recent innovations in laser additive manufacturing of titanium alloys. *Int. J. Extrem. Manuf.* **6**, 032001 (2024).
17. Zilnyk, K. D. et al. Misorientation distribution between martensite and austenite in Fe-31 wt%Ni-0.01 wt%C. *Acta Mater.* **143**, 227–236 (2018).
18. Toji, Y. et al. Effect of Si on the acceleration of bainite transformation by pre-existing martensite. *Acta Mater.* **116**, 250–262 (2016).
19. Li, X. et al. Quantification of complex-phase steel microstructure by using combined EBSD and EPMA measurements. *Mater. Charact.* **142**, 179–186 (2018).
20. Baek, M. S. et al. Quantitative phase analysis of martensite-bainite steel using EBSD and its microstructure, tensile and high-cycle fatigue behaviors. *Mater. Sci. Eng. A* **785**, 139375 (2020).
21. Ping, D. H. et al. A transition of ω-Fe3C → ω′-Fe3C → θ′-Fe3C in Fe-C martensite. *Sci. Rep.* **10**, 6081 (2020).
22. Zhang, M. X. et al. Accurate orientation relationships between ferrite and cememtite in pearlite. *Scr. Mater.* **37**, 2009–2015 (1997).
23. Lai, M. J. et al. ω phase acts as a switch between dislocation channeling and joint twinning- and transformation-induced plasticity in a metastable β titanium alloy. *Acta Mater.* **151**, 67–77 (2018).
24. Li, M. et al. Novel insight into the formation of α″-martensite and ω-phase with cluster structure in metastable Ti-Mo alloys. *Acta Mater.* **164**, 322–333 (2019).
25. Peng, H. et al. Deformation-induced interfacial-twin-boundary ω-phase in an Fe48Mn37Al15 body-centered cubic metastable alloy. *J. Mater. Sci. Technol.* **146**, 252–258 (2023).
26. Kuts, M. *Handbook of Materials Selection* (John Wiley & Sons, 2002).
27. Klueh, R. L. *ASM Handbook Volume 1 Properties and selection: irons, steels, and high performance alloys*. (ASM International, 2005).
28. Juhas, M. C. et al. Effect of prestrain on the mechanical properties of eutectoid steel. *Metall. Mater. Trans. A* **14**, 1379–1388 (1983).
29. Behera, S. et al. Tailoring the processing route to optimize the strength–toughness combination of pearlitic steel. *Metall. Mater. Trans. A* **53**, 3853–3868 (2022).
30. Altan ÖZbek, N. et al. Effects of tempering heat treatment temperatures on mechanical properties of carbon steels. *Gazi m.ühendis. bilim. derg.* **7**, 17–25 (2021).
31. Mishra, A. et al. Structure–property correlation of AISI 1080 steel subjected to cyclic quenching treatment. *Mater. Sci. Eng. A* **646**, 169–181 (2015).
32. Mishra, S. et al. Simultaneous enhancement of ductility and strength in AISI 1080 steel through a typical cyclic heat treatment. *Mater. Sci. Eng. A* **688**, 262–271 (2017).
33. La, P. et al. Effect of substrates on microstructure and mechanical properties of nano-eutectic 1080 steel produced by aluminothermic reaction. *Mater. Charact.* **92**, 84–90 (2014).
34. Garbarz, B. et al. Effect of pearlite morphology on impact toughness of eutectoid steel containing vanadium. *Mater. Sci. Technol.* **4**, 328–334 (1988).
35. Weiss, B. Z. *Maraging Steels—Structure, Properties and Applications* in *Specialty Steels and Hard Materials* (eds N. R. Comins & J. B. Clark) 35-54 (Pergamon, 1983).
36. Li, K. et al. Additive manufacturing of ultra-high strength steels: A review. *J. Alloy. Compd.* **965**, 171390 (2023).
37. Tan, Q. et al. Rationalization of brittleness and anisotropic mechanical properties of H13 steel fabricated by selective laser melting. *Scr. Mater.* **214**, 114645 (2022).
38. Mooney, B. et al. Plastic anisotropy of additively manufactured maraging steel: influence of the build orientation and heat treatments. *Addit. Manuf.* **25**, 19–31 (2019).
39. Bai, Y. et al. Effect of heat treatment on the microstructure and mechanical properties of maraging steel by selective laser melting. *Mater. Sci. Eng. A* **760**, 105–117 (2019).
40. Sun, G. et al. Evaluation of defect density, microstructure, residual stress, elastic modulus, hardness and strength of laser-deposited AISI 4340 steel. *Acta Mater.* **84**, 172–189 (2015).
41. Jelis, E. et al. Process evaluation of AISI 4340 steel manufactured by laser powder bed fusion. *JMEP* **27**, 63–71 (2018).
42. Kumar, A. et al. Mechanical properties of nanostructured bainitic steels. *Materialia* **15**, 101034 (2021).
43. Bhadeshia, H. Nanostructured bainite. *Proc. R. Soc. A: Math. Phys. Eng. Sci.* **466**, 3–18 (2010).
44. Kumar, A. et al. Compositional design of high strength nanostructured bainite. *Mater. Res. Express* **6**, 026526 (2018).
45. Kumar, A. et al. Toughness dependence of nano-bainite on phase fraction and morphology. *Mater. Sci. Eng. A* **729**, 439–443 (2018).
46. Todaro, C. J. et al. Grain structure control during metal 3D printing by high-intensity ultrasound. *Nat. Commun.* **11**, 142 (2020).
47. Martin, J. H. et al. 3D printing of high-strength aluminium alloys. *Nature* **549**, 365 (2017).
48. Zhang, D. et al. Additive manufacturing of ultrafine-grained high-strength titanium alloys. *Nature* **576**, 91–95 (2019).
49. Wang, Y. M. et al. Additively manufactured hierarchical stainless steels with high strength and ductility. *Nat. Mater.* **17**, 63 (2017).
50. Tan, Q. Y. et al. Unravelling the roles of TiN-nanoparticle inoculant in additively manufactured 316 stainless steel. *J. Mater. Sci. Technol.* **175**, 153–169 (2024).
51. Özbilen, S. Satellite formation mechanism in gas atomised powders. *Powder Met.* **42**, 70–78 (1999).
52. Tan, Q. et al. A novel strategy to additively manufacture 7075 aluminium alloy with selective laser melting. *Mater. Sci. Eng. A* **821**, 141638 (2021).
53. Tan, Q. *Data from "High performance plain carbon steels obtained through 3D-printing"* https://doi.org/10.6084/m9.figshare.27368010 (2024).

Acknowledgements

This work was supported by the Australian Research Council (ARC, grant number: DP210103162, recipient: M.X.Z.). Q.T. thanks Australian Microscopy & Microanalysis Research Facility at the Centre for Microscopy and Microanalysis (CMM), The University of Queensland for the facilities and technical assistance.

Author contributions

Q.T., H.C., and M.X.Z. conceived the research. Q.T. and H.C. carried out the main experiments. M.X.Z. and C.H. offered supervisory guidance and project administration. G.L. and F.W. contributed to feedstock preparation and sample processing. Q.T. and G.L. conducted hardenability test. V.L. contributed to the evaluation of cracking and distortion behavior.

Q.T., H.C., and Y.Y. prepared XRD, EBSD, and TEM samples, and conducted corresponding characterizations. Q.T. and H.C. conducted mechanical testing. X.C., M.X.Y., and Q.Z. contributed idea for the research and analysed the EBSD data. Q.T. and M.Z. conducted crystallographic analysis. Q.T. C.H. and M.X.Z. analysed the data and drafted the initial manuscript. All authors contributed to the discussion of the results and revision on the manuscript.

Competing interests
The authors declare no competing interests.

Additional information
Supplementary information The online version contains supplementary material available at https://doi.org/10.1038/s41467-024-54507-4.

Correspondence and requests for materials should be addressed to Christopher Hutchinson or Ming-Xing Zhang.

Peer review information *Nature Communications* thanks Hao Chen, who co-reviewed with Wenhua Wu, Bilal Gökce, Pedro Rivera and the other, anonymous, reviewer(s) for their contribution to the peer review of this work. A peer review file is available.